Finite element analysis of ionic liquid gel soft actuator*

Bin He(何斌)†, Cheng-Hong Zhang(张成红), and An Ding(丁安)

College of Electronics and Information Engineering, Tongji University, Shanghai 201804, *China*

(Received 8 June 2017; revised manuscript received 8 September 2017; published online 20 November 2017)

A new type of soft actuator material-ionic liquid gel (ILG), which consists of HEMA, $BMIMBF_4$, and TiO_2, can be transformed into gel state under the irradiation of ultraviolet (UV) light. In this paper, Mooney–Rivlin hyperelastic model of finite element method is proposed for the first time to study the properties of the ILG. It has been proved that the content of TiO_2 has a great influence on the properties of the gel, and Young's modulus of the gel increases with the increase of its content, despite of reduced tensile deformation. The results in this work show that when the TiO_2 content is 1.0 wt%, a large tensile deformation and a strong Young's modulus can be obtained to be 325% and 7.8 kPa, respectively. The material parameters of ILG with TiO_2 content values of 0.2 wt%, 0.5 wt%, 1.0 wt%, and 1.5 wt% are obtained, respectively, through uniaxial tensile tests, including C_{10}, C_{01}, C_{20}, C_{11}, C_{02}, C_{30}, C_{21}, C_{12}, and C_{03} elements. In this paper, the large-scaled general finite element software ANSYS is used to simulate and analyze the ILG, which is based on SOLID186 element and nonlinear hyperelastic Mooney–Rivlin model. The finite element simulation analysis based stress-strain curves are almost consistent with the experimental stress–strain curves, and hence the finite element analysis of ILG is feasible and credible. This work presents a new direction for studying the performance of soft actuator for the ILG, and also contributes to the design of soft robot actuator.

Keywords: ionic liquid gel (ILG), soft actuator, Mooney–Rivlin model, finite element analysis

PACS: 61.41.+e, 47.11.Fg, 11.10.Lm **DOI:** 10.1088/1674-1056/26/12/126102

1. Introduction

Due to high environment adaptability and low pressure impedance characteristics, soft robot has broad application prospects in the fields of biology, medicine, etc. The adoption of electro active polymer (EAP) material has become a hot research topic these years. Electrochemical actuator has been further developed in the last decades due to their desired mechanical properties exhibited in intelligent robots, which has been an alternative to air and fluid deriving equipment.[1–4] The flexible ionic conductivity of the ILG is more suitable building blocks for the evolution of actuators due to its chemical stability, thermal stability and simpler ion transport.[5–7]

Non-covalent interactions provide the gels with very high mechanical strength and excellent self-healing ability of supramolecular materials.[8–10] On the basis of these studies, we use TiO_2 nanoparticles to fabricate supramolecular nanocomposites with electrochemical behavior of mechanical strength ionogel polymer and ionic liquid.

With the good development of numerical means, finite element analysis has been one of the most effective and abundant information extraction methods to evaluate and optimize robot design. Analytical model can therefore be greatly simplified, hence the computational efficiency is greatly increased. The most critical drawback is that the ignorance of the nonlinear and constitutive model and simplification of the computational model lead to a coarse solution.[11,12] The numerical simulations offer a sufficient insight for every single case during the general soft robot approach.

To reduce the experimental cost and time consumption,we perform a systematic analysis of the ILG based on numerical simulations, and verify the accuracy of the finite element calculation, and also make some contribution to the development of the ILG in soft robot. The numerical simulation results are matched with the corresponding experiments, and hence the validity of the finite element model is proved.

This single behavior can be directly applied to some simple geometric numerical method, which takes into consideration some specific features of analysis process, and the finite element method has therefore become one of the most effective tools for process modeling, including ILG.[13–15]

2. Fabrication of ILG

In our experiments, the ILGs are composed of1-butyl-3-methylimidazolium tetrafluoroborate ($BMIMBF_4$), hydroxyethyl methacrylate (HEMA) and TiO_2 nanoparticles, with mass of 890 mg, 100 mg, and 10 mg, respectively. The mixed solution is then placed into a magnetic stirrer to stir, forming a suspension. Following that the sample was placed on the ML-3500C Maxima-type cold light source, i.e., an ultra high intensity UV curing lamp, for polymerization.

Figure 1(a) shows a comparison between the morphologies of the ionic liquid before and after the gel is formed, the

*Project supported by the National Natural Science Foundation of China (Grant Nos. 51538009 and 51605334) and the Natural Science Foundation of Shanghai Municipality, China (Grant No. 08002360285).

†Corresponding author. E-mail: hebin@tongji.edu.cn

© 2017 Chinese Physical Society and IOP Publishing Ltd

right figure shows the liquid state, and the left figure shows the solid state formed after polymerization. The schematic diagram of the generating principle is illustrated in Figs. 1(b)–1(d). Under the irradiation of UV light, the polymerization reaction occurs in HEMA, polymer matrix cross-linked with each other, and thus a porous network structure is formed.[16]

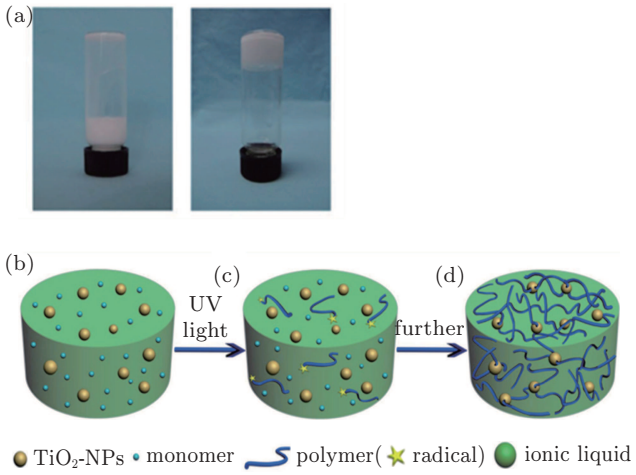


Fig. 1. (color online) Proposed mechanism of the $BMIMBF_4$-based ionogel under UV light. (a) ILG solution and ILG respectively. (b) The ILG solution inclusion $BMIMBF_4$, HEMA, and TiO_2 nanoparticles. (c) Polymerization initiated by the TiO_2 nanoparticles. (d) HEMA and TiO_2 nanoparticles cross coupled to form a three-dimensional (3D) network.

3. Material nonlinearity and parameters

The morphology analysis of freeze-dried sample using scanning electron microscopy (SEM) shows that the porous microstructure occurs in the ubiquitous ionogels. Distilled water was used to replace the ILG internal ionic liquid, after the freeze-drying treatment, S4800 Hitachi type high resolution field emission scanning electron microscope was used to scan the section. Figure 2 shows that under a magnification of 5000, the spatial structure of the ionic liquid carrier HEMA is the typical 3D porous structure, and its matrix is cross-linked to each other to form a 3D support skeleton, offering good mechanical strength and self-repair performance.

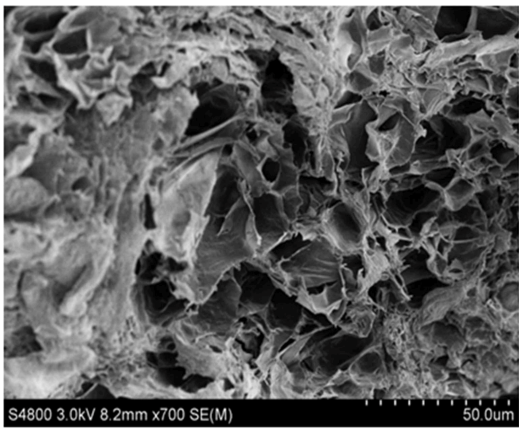


Fig. 2. SEM image of a freeze-dried $BMIMBF_4$-based gel after replacing the ionic liquid with water.

From the image of the ILG under the SEM, it can be seen that the material possesses an irregular network structure, which is a nonlinear material. The nonlinear properties of the material are also validated by stress-strain curves of the experimental results and simulation results.

3.1. Hyperelastic nonlinearity

Assuming that the ILG is an isotropic incompressible hyperelastic body, the following assumptions are made based on the theory of continuum mechanics to study its mechanical properties.

(i) If there is a unit mass of material strain energy function W, it is an analytic function of the strain tensor of the natural state, termed hyperelastic hypothesis. If the time rate of change of W is equal to that of the power of the stress, the material is called the hyperelastic material. The mechanical properties of the hyper elastic material are described by the strain energy density function W, which has many functions.[17,18]

(ii) Isotropic assumption.

(iii) It is assumed that the volumes of the material before and after deformation are the same.

Parameters λ_1, λ_2, λ_3 are set to be in the three directions of the main (extension) deformation rate, respectively, given by

$$\lambda_1 = \frac{x}{x_0}, \quad \lambda_2 = \frac{y}{y_0}, \quad \lambda_3 = \frac{d}{d_0}, \tag{1}$$

where, x, y, and d are the dimensions of length, width, and thickness direction, respectively. x_0, y_0, and d_0 are the initial sizes before the deformation.

Because the material is not compressible, the volumes of the deformation before and after are the same, giving

$$xyd = x_0 y_0 d_0, \tag{2}$$

$$\frac{xyd}{x_0 y_0 d_0} = \lambda_1 \lambda_2 \lambda_3 = 1. \tag{3}$$

3.2. Hyperelastic stress

Based on comparisons of various hyperelastic constitutive models, Mooney–Rivlin model is selected. Mechanical property of ionic gel material is then studied using Mooney–Rivlin formula, which has been termed nonlinear finite element of ionic gels in previous study.[19,20]

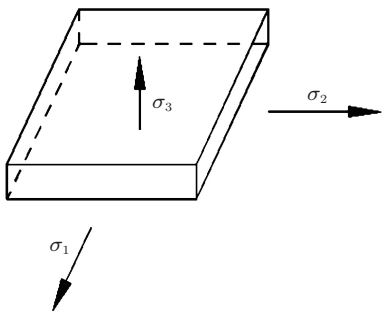


Fig. 3. Stress in each direction.

The strain energy function, i.e., Mooney–Rivlin model equation is as follows:

$$W = \sum_{i \neq j} c_{ij}(I_1 - 3)^i (I_2 - 3)^j. \tag{4}$$

The form of the strain energy potential is given by

$$\begin{aligned} W \;=\; & c_{10}(I_1-3) + c_{01}(I_2-3) + c_{20}(I_1-3)^2 \\ & + c_{11}(I_1-3)(I_2-3) + c_{02}(I_2-3)^2 + c_{30}(I_1-3)^3 \\ & + c_{21}(I_1-3)^2(I_2-3) + c_{12}(I_1-3)(I_2-3)^2 \\ & + c_{03}(I_2-3)^3, \end{aligned} \tag{5}$$

where the required input parameters c_{10}, c_{01}, c_{20}, c_{11}, c_{02}, c_{30}, c_{21}, c_{12}, and c_{03} are the material constants.

The physical properties are mainly described by the strain energy function. Each model is in a special form of the strain energy function. Once the form of the strain energy function W is determined, the Cauchy stress tensor P can be given by

$$\sigma = -pI + 2\frac{\partial W}{\partial I_1}B - 2\frac{\partial W}{\partial I_2}B^{-1}, \tag{6}$$

where I is the unit tensor, which is the left Gauss deformation tensor, and P is the hydrostatic pressure introduced by the incompressible assumption,

$$\begin{cases} I_1 = B, \\ I_2 = \dfrac{1}{2}[I_1^2 - \mathrm{tr}(B^2)], \\ I_3 = \det B. \end{cases} \tag{7}$$

The relationship between the invariants and principal elongation is a function of B:

$$\begin{cases} I_1 = \lambda_1^2 + \lambda_2^2 + \lambda_3^2, \\ I_2 = \lambda_1^2\lambda_2^2 + \lambda_2^2\lambda_3^2 + \lambda_1^2\lambda_3^2, \\ I_3 = \lambda_1^2\lambda_2^2\lambda_3^2, \end{cases} \tag{8}$$

and hence the isotropic and incompressible deformation process of ILG is given as

$$\sqrt{I_3} = \lambda_1\lambda_2\lambda_3 = 1. \tag{9}$$

According to formulas (6) and (8), it can be obtained that

$$\sigma_i = 2\left[\lambda_i^2\frac{\partial W}{\partial I_1} - \frac{1}{\lambda_i^2}\frac{\partial W}{\partial I_2}\right] - p, \tag{10}$$

where I_1, I_2, and I_3 are the relative changes of the length, surface area and volume of the elastomer, respectively.

Also,

$$\sigma_1 = 2\left(\lambda_1^2\frac{\partial W}{\partial I_1} - \frac{1}{\lambda_1^2}\frac{\partial W}{\partial I_2}\right) - p, \tag{11}$$

$$\sigma_2 = 2\left(\lambda_2^2\frac{\partial W}{\partial I_1} - \frac{1}{\lambda_2^2}\frac{\partial W}{\partial I_2}\right) - p, \tag{12}$$

$$\sigma_3 = 2\left(\lambda_3^2\frac{\partial W}{\partial I_1} - \frac{1}{\lambda_3^2}\frac{\partial W}{\partial I_2}\right) - p, \tag{13}$$

where $\partial W/\partial I_1$ and $\partial W/\partial I_2$ are the partial differentials of the strain energy function W with respect to I_1 and I_2, respectively; σ_1, σ_2, and σ_3 are the stresses in the x, y, z directions, respectively.

Because only axial tensile deformation is considered, the stresses in the other two directions are zero, i.e.,

$$\sigma_2 = \sigma_3 = 0, \tag{14}$$

giving

$$I_1 = \lambda_1^2 + \frac{2}{\lambda_1}, \tag{15}$$

$$I_2 = \frac{1}{\lambda_1^2} + 2\lambda_1. \tag{16}$$

The partial differentials of the strain energy function W with respect to I_1 and I_2 are given by

$$\begin{aligned} \frac{\partial W}{\partial I_1} \;=\; & c_{10} + 2c_{20}(I_1-3) + c_{11}(I_2-3) + 3c_{30}(I_1-3)^2 \\ & + 2c_{21}(I_1-3)(I_2-3) + c_{12}(I_2-3)^2 = M, \end{aligned} \tag{17}$$

$$\begin{aligned} \frac{\partial W}{\partial I_2} \;=\; & c_{01} + 2c_{02}(I_2-3) + c_{11}(I_1-3) + 3c_{03}(I_2-3)^2 \\ & + 2c_{12}(I_1-3)(I_2-3) + c_{21}(I_1-3)^2 = N. \end{aligned} \tag{18}$$

Therefore,

$$\sigma_1 = 2\left(\lambda_1^2 - \frac{1}{\lambda_1}\right)\left(M + \frac{1}{\lambda_1}N\right). \tag{19}$$

One of the key parts of finite element analysis is to simulate the accuracy of the material parameters.The TiO_2 content values are set to be 0.2 wt%, 0.5 wt%, 1.0 wt%, and 1.5 wt% ILG, respectively, and hence form 4 groups of material parameters.

4. FEM model for forming simulations

The main purpose of the numerical simulations is to seek an effective analytical tool for studying the ILGs in detail to support the design of soft robots. The details of the whole finite element model including ILG elements are depicted in Fig. 4, corresponding to its geometric model.[21–23]

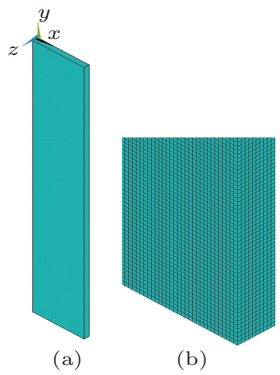


Fig. 4. (color online) (a) Geometric model; (b) Finite element model.

The model size is 30 mm×5 mm×(0.5 mm or 1.0 mm), and the stress–strain curves are computed under various values of TiO_2 content, and the force-displacement curves are thus can be calculated.

4.1. Geometry, materials, program settings

The geometric model shown in Fig. 4 has an ILG size of 25-mm long, 5-mm wide, and 0.5-mm or 1-mm thick.

The first analysis of the finite element model required for the deformation must be globally acceptable hyperelastic model, and the general characteristics of the ILG hyperelastic model can therefore be captured.

According to the uniaxial tensile tests, the values of C_{10}, C_{01}, C_{20}, C_{11}, C_{02}, C_{30}, C_{21}, C_{12}, and C_{03} are obtained and summarized in Table 1.

Due to nonlinear hyperelastic calculation, maximum ILG deformation strain turns to be as high as approximately 430%. For better convergence, in the analysis of the ANSYS finite element simulations, the load step is set to be 2000, the minimum load step is set to be 100, the maximum load step is set to be 1000, and the maximum iteration is set to be 100.

Table 1. Mechanical properties of the $BMIMBF_4$-based ionogels with different TiO_2 concentrations.

TiO_2/wt%	C_{10}	C_{01}	C_{20}	C_{11}	C_{02}	C_{30}	C_{21}	C_{12}	C_{03}
0.2	−12.2807	18.3417	5.95×10^{5}	-7.81×10^{-3}	3.0927	6.54×10^{-13}	-4.8110^{-10}	-1.4710^{-5}	1.9210^{-3}
0.5	−18.5854	27.8485	-2.3210^{-5}	0.0218	4.6449	-2.9110^{-12}	1.5610^{-9}	5.5210^{-6}	-5.4410^{-3}
1.0	36.3521	−53.9507	9.3010^{-5}	0.0122	−9.0515	-1.3810^{-11}	7.7010^{-9}	-2.4810^{-5}	-2.9710^{-3}
1.5	660.293	−986.710	0.0272	−4.3149	−158.571	-3.1010^{-10}	1.2110^{-7}	6.8310^{-3}	1.0694

4.2. Boundary conditions, load

The constraint conditions of all degrees of freedom (DOF) of the structure are clamped and fixed by the constant boundary nodes. When the finite element is calculated, the upper end of the ILG is fixed, and the lower end of the ILG is loaded. In order to obtain the stress-strain curve of each model, 10 different load conditions are calculated in the corresponding model.

4.3. Mesh settings

For mesh settings, the different element types are analyzed in the model development process. With higher values in the hyperelastic nonlinear calculation, SOLID186 element gives a better convergence. The size of the elements in the mesh is calculated to guarantee the convergence of the results. The ANSYS finite element analysis model size is 30 mm×5 mm×(0.5 mm or 1.0 mm). By analyzing the convergence and time consumption of simulation calculation, the finite element grid size is set to be 0.05 mm×0.05 mm×0.05 mm, which are 6×10^5 or 1.2×10^5 elements.

5. Numerical results

In Fig. 5, when the content of TiO_2 is 0.2 wt%, the simulation results are analyzed: when $f = 1.49$ mN, the deformation is 6.72 mm; when $f = 8.56$ mN, the deformation is 28.56 mm; when $f = 12.68$ mN, the deformation is 59.32 mm; when $f = 13.92$ mN, the deformation is 93.94 mm; when $f = 13.02$ mN, the deformation is 130.16 mm.

Figure 6(a) shows that the ILG is thick and short before the load is applied. As the tensile load increases, the ILG becomes longer and thinner, which is shown in panels (b) and (c). Figure 5(a)–5(e) are the simulation results of ILG under different loads, showing that with the tensile load increasing, the simulation results are consistent with the experiment results, too. It can be seen in Figs. 5 and 6 that the ILG is consistent with the assumption that the material is incompressible, as shown in Eq. (9).

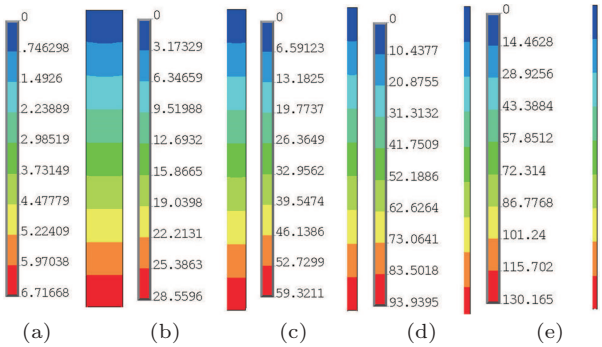


Fig. 5. (color online) Calculation results for TiO_2 content of 0.2 wt% and ILG thickness of 0.5 mm.

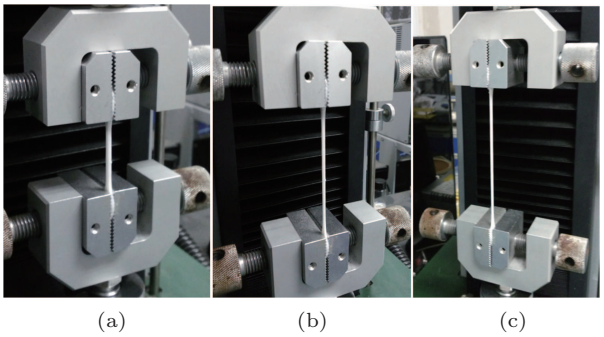


Fig. 6. (color online) Change of the ILG.

Table 2. Calculation results for TiO_2 content of 0.2 wt% and ILG thickness of 0.5 mm.

Force/mN	1.49	8.56	12.68	13.92	13.02
Deformation/mm	6.72	28.56	59.32	93.94	130.16

In Fig. 8, when the content of TiO_2 is 0.2 wt%, the simulation results are analyzed: when $f = 4.34$ mN, the deformation is 5.92 mm; when $f = 15.12$ mN, the deformation is 24.57 mm; when $f = 24.41$ mN, the deformation is 51.11 mm; when $f = 26.55$ mN, the deformation is 81.57 mm; when $f = 27.93$ mN, the deformation is 113.72 mm.

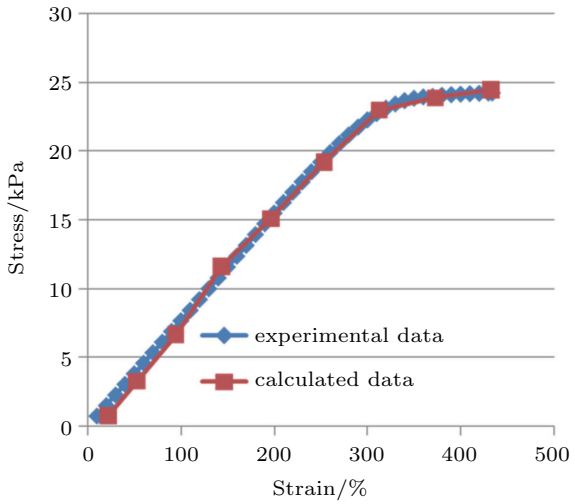


Fig. 7. (color online) Comparison of experimental data with calculated data, for TiO_2 content of 0.2 wt% and ILG thickness of 0.5 mm.

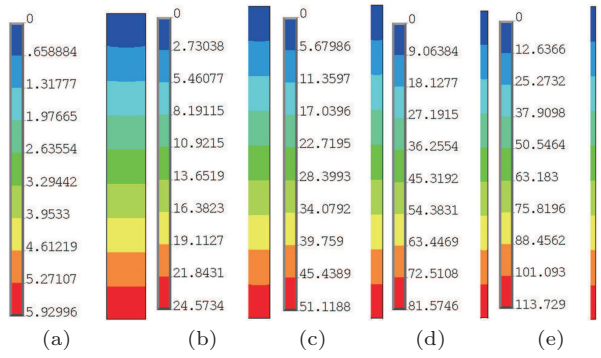


Fig. 8. (color online) Calculation results for TiO_2 content of 0.2 wt% and ILG thickness of 1.0 mm.

Table 3. Calculation results for TiO_2 content of 0.2 wt% and ILG thickness of 1.0 mm.

Force/mN	4.34	15.12	24.41	26.55	27.93
Deformation/mm	5.92	24.57	51.11	81.57	113.72

In Fig. 10, when the content of TiO_2 is 0.5 wt%, the simulation results are analyzed: when $f = 7.21$ mN, the deformation is 6.01 mm; when $f = 25.32$ mN, the deformation is 25.10 mm; when $f = 35.49$ mN, the deformation is 52.62 mm; when $f = 37.56$ mN, the deformation is 84.43 mm.

Table 4. Calculation results for TiO_2 content of 0.5 wt% and ILG thickness of 0.5 mm.

Force/mN	7.21	25.32	35.49	37.56
Deformation/mm	6.01	25.10	52.62	84.43

In Fig. 12, when the content of TiO_2 is 0.5 wt%, the simulation results are analyzed: when $f = 11.62$ mN, the deformation is 4.86 mm; when $f = 40.70$ mN, the deformation is 19.39 mm; when $f = 69.44$ mN, the deformation is 40.42 mm; when $f = 74.42$ mN, the deformation is 65.54 mm; when $f = 76.14$ mN, the deformation is 92.74 mm.

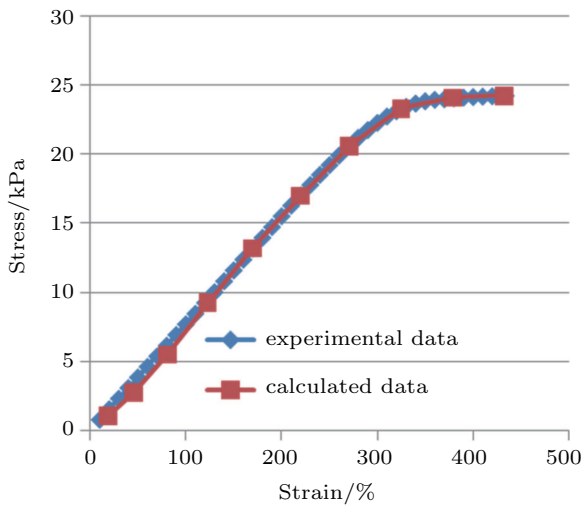


Fig. 9. (color online) Comparison of experimental data with calculated data for TiO_2 content of 0.2 wt% and ILG thickness of 1.0 mm.

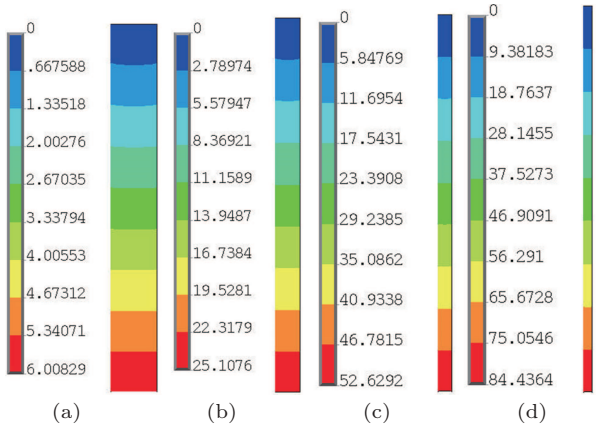


Fig. 10. (color online) Calculation results for TiO_2 content of 0.5 wt% and ILG thickness of 0.5 mm.

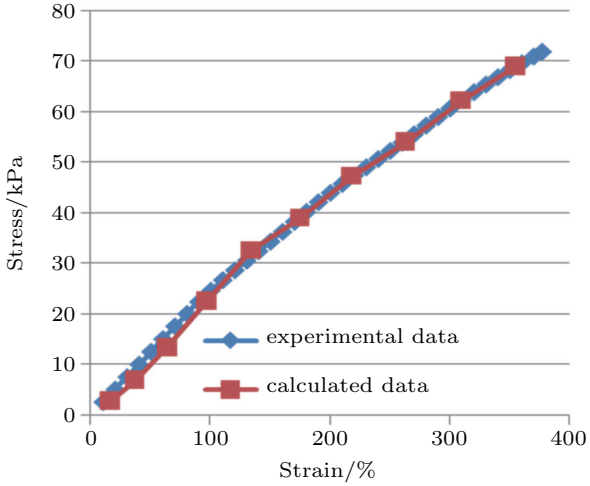


Fig. 11. (color online) Comparison of experimental data with calculated data for TiO_2 content of 0.5 wt% and ILG thickness of 0.5 mm.

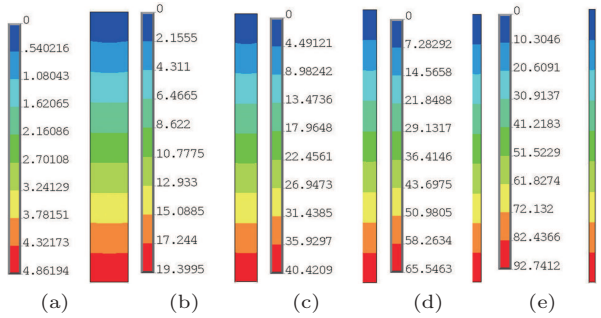


Fig. 12. (color online) Calculation results for TiO_2 content of 0.5% and ILG thickness of 1.0 mm.

Table 5. Calculation results for TiO_2 content of 0.5 wt% and ILG thickness of 1.0 mm.

Force/mN	11.62	40.70	69.44	74.42	76.14
Deformation/mm	4.86	19.39	40.42	65.54	92.75

It can be seen that the ILGhas a TiO_2 content value of 0.2 wt% in Figs. 7 and 9, and the value is 0.5 wt% in Figs. 11 and 13. Both the length and the width of the ILG are fixed, the ILG thickness is 0.5 mm in Figs. 7 and 11, and the value is 1.0 mm in Figs. 9 and 13. The simulation results show that the stress-strain curve in Fig. 7 is substantially the same as the stress-strain curve in Fig. 9, and the stress-strain curve in Fig. 11 is substantially the same as the stress-strain curve in Fig. 13. The thickness of the ILG therefore has no effect on the hyperelastic nonlinear calculation and affects the magnitude of the load only.

According to Figs. 7, 9, 11, and 13, it can be seen that the calculated thickness has no effect on the nonlinearity of the finite element. The ILG with a thickness of 0.5 mm is then calculated.

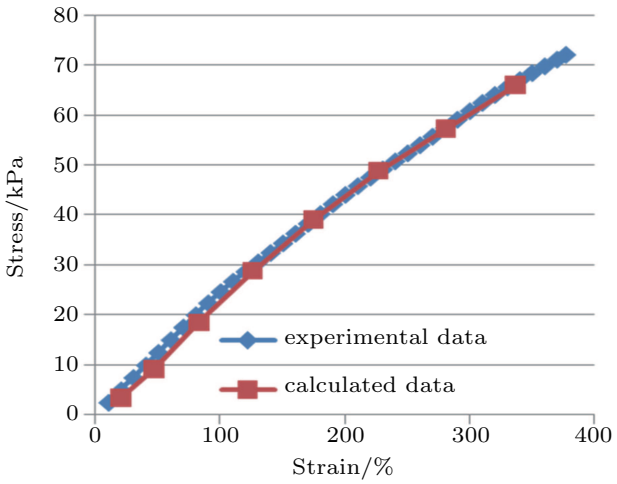


Fig. 13. (color online) Comparison of experimental data with calculated data for TiO_2 content of 0.5 wt% and ILG thickness of 1.0 mm.

In Fig. 14, when the content of TiO_2 is 1.0 wt%, the simulation results are analyzed: when $f = 11.90$ mN, the deformation is 4.61 mm; when $f = 40.35$ mN, the deformation is 18.14 mm; when $f = 73.60$ mN, the deformation is 37.56 mm; when $f = 79.69$ mN, the deformation is 60.82 mm; when $f = 80.01$ mN, the deformation is 86.05 mm.

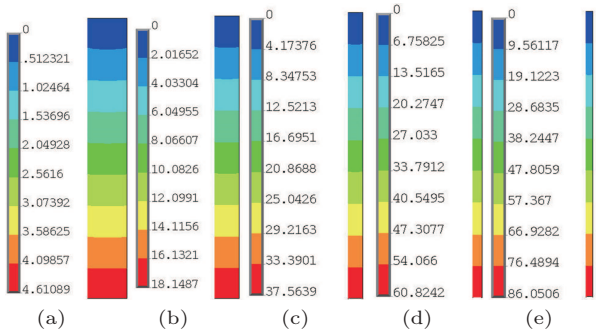


Fig. 14. (color online) Calculation results for TiO_2 content of 1.0 wt% and ILG thickness of 0.5 mm.

Table 6. Calculation results at TiO_2 content for 1.0 wt% and ILG thickness of 0.5 mm.

Force/mN	11.90	40.35	73.60	79.69	80.01
Deformation/mm	4.61	18.14	37.56	60.82	86.05

In Fig. 16, when the content of TiO_2 is 1.5 wt%, the simulation results are analyzed: when $f = 23.67$ mN, the deformation is 2.64 mm; when $f = 74.56$ mN, the deformation is 9.43 mm; when $f = 136.13$ mN, the deformation is 18.65 mm; when $f = 164.13$ mN, the deformation is 30.41 mm; when $f = 169.05$ mN, the deformation is 44.31 mm.

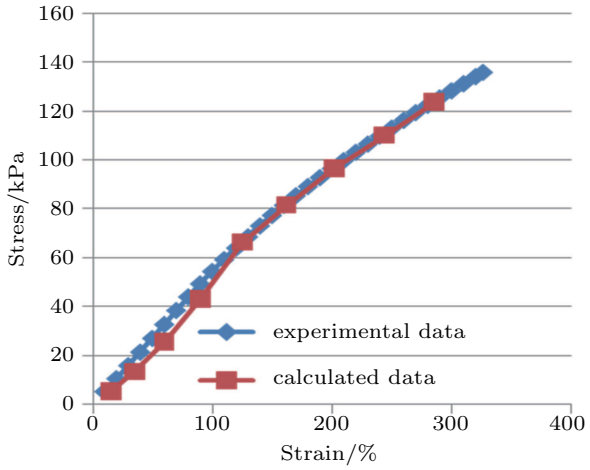


Fig. 15. (color online) Comparison of experimental data with calculated data for TiO_2 content of 1.0 wt% and ILG thickness of 0.5 mm.

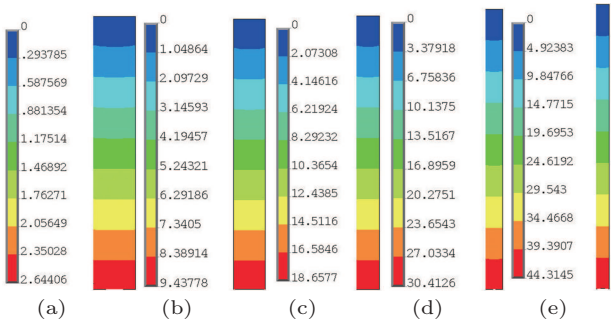


Fig. 16. (color online) Calculation results for TiO_2 content of 1.5 wt% and ILG thickness of 0.5 mm.

Table 7. Calculation results for TiO_2 content of 1.5 wt% and ILG thickness of 0.5 mm.

Force/mN	23.67	74.56	136.13	164.13	169.05
Deformation/mm	2.64	9.43	18.65	30.41	44.31

It can be seen in Figs. 7, 11, 15, and 17 that the content values of TiO_2 are 0.2 wt%, 0.5 wt%, 1.0 wt%, and 1.5 wt%, respectively. From the stress-strain curve, during the initial period (with a strain less than 100%), the error between the experimental results and the finite element simulation results is less than 10%, and both the errors of the remaining experimental results and the errors of the finite element calculation results are less than 5%.

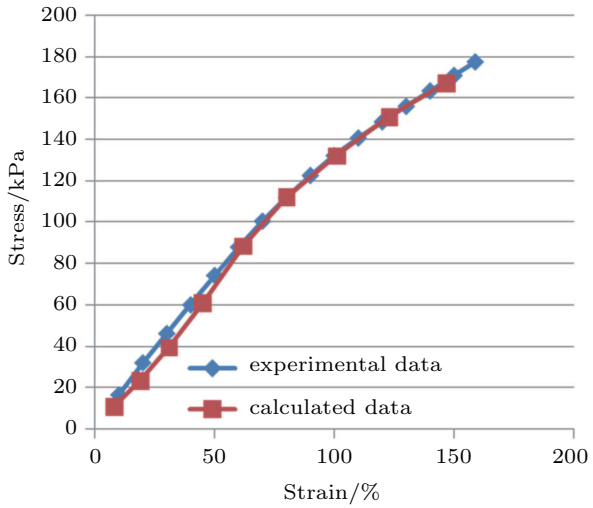


Fig. 17. (color online) Comparison of experimental data with calculated data for TiO_2 content of 1.0 wt% and ILG thickness of 0.5 mm.

6. Experimental results

Figure 18 shows a series of pictures for TiO_2 content of 1.5 wt% from the applied load to the fracture process. Before the load is applied in Fig. 18(a), a material deformation under a load in Fig. 18(b), and the material is broken in Fig. 18(c). Figure 19 shows the stress-strain curves for TiO_2 content values of 0.2 wt%, 0.5 wt%, 1.0 wt%, and 1.5 wt%, respectively. According to the analysis results summarized and illustrated above, it can be seen that the simulation results are consistent with the experimental results.

The ionogel $BMIMBF_4$ shows a high level of hyperelastic toughness when the maximum deformation and a tensile limit is close to 430%. Tensile tests show that the tensile properties of the gel can be enhanced by increasing the TiO_2 content. In the tensile tests, Young's modulus is an optimum mechanical index for the synthesis condition. Increasing the quantity of TiO_2 nanoparticles will generate more cross-linking sites and higher conversion, which will contribute to the final mechanical properties.[24] The optimized quantity of TiO_2 nanoparticles is 1.0 wt%, considering the data that have been collected so far and the relatively large tensile deformation and tensile strength.

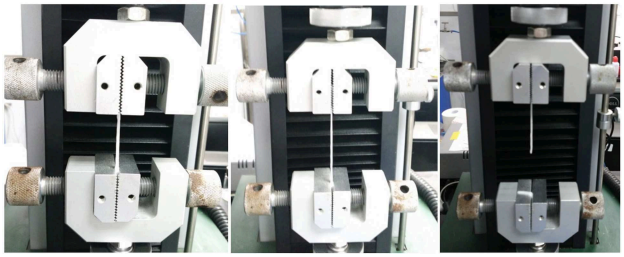


Fig. 18. (color online) Uniaxial tensile test.

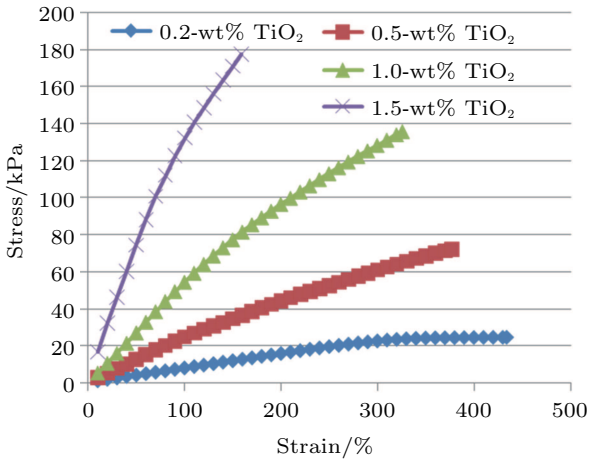


Fig. 19. (color online) ILG tensile test.

7. Discussion

In the analysis of ILG, SOLID186 element with finer mesh sizes can be used to achieve better simulation results. At the beginning of the simulation analysis, a small time step is necessary for system convergence. An appropriate macro or user subroutine is built up in the form of the parameters of the table and allows the restart of analysis at every time step.

The simulation results show that the finite element model has a good correlation with the corresponding experimental data. It is pointed out that the average error between the finite element calculation and the experimental data is small, showing the design potential of this method for soft robots.[25,26] The finite element model requires the input of some mechanical properties of the ILG. In this paper, a standard uniaxial stretch method is used to measure the required ILG properties.

As shown in Fig. 2, the ILG is a network structure. However, in the process of finite element simulations, it is assumed that the ILG is a hyperelastic nonlinear network structure. The simulation results of the finite element are almost the same as the experimental results, and the result of the finite element simulation is therefore credible.

8. Conclusions

ANSYS structure program can be used to model the formation process of the soft robot by hyperelastic nonlinear calculation of the ILGs. In this paper, the model of the ILG

is built up based on the hyperelastic nonlinear finite element model, and the results show that Mooney–Rivlin model can be well adapted to the constitutive relation of the material.[27] The main advantage of the ILG is that it can obtain stress-strain curve, which can therefore obtain the performance parameters of the material in a relatively short time.

In the future, the investigations on the generalized algorithm to recognize the mechanical properties of ILGs are carried out. Finally, it is pointed out that all the results in this work show a good correlation between the 3D theoretical assumptions and the experimental conditions. The achievements made in this work will contribute to the design of future soft robot actuator.

References

[1] Pelrine R, Kornbluh R, Pei Q B and Joseph J 2000 *Science* **287** 836
[2] Hammock M L, Chortos A, Tee B C K, Tok J B H and Bao Z A 2013 *25th Anniversary Adv. Mater.* **25** 5997
[3] Feinberg A W, Feigel A, Shevkoplyas S S, Sheehy S, Whitesides G M and Parker K K 2007 *Science* **317** 1366
[4] Gu W, Wei J and Yu Y L 2016 *Chin. Phys. B* **25** 096103
[5] Buchtova' N, Guyomard-Lack A and Le Bideau J 2014 *Green Chem.* **16** 1149
[6] Le Bideau, J, Viau L and Vioux A 2011 *Chem. Soc. Rev.* **40** 907
[7] Zhang W, Chen L Z, Zhang J M and Huang Z G 2017 *Chin. Phys. B* **26** 048801
[8] Zhang M M, Xu D H, Yan X Z, Chen J Z, Dong S Y, Zheng B and Huang F H 2012 *Angew. Chem. Int. Ed.* **51** 7011
[9] Zhang D, Yang J H, Bao S, Wu Q S and Wang Q G 2013 *Sci. Rep.* **3** 1399
[10] Zhang J H, Mao X L, Liu Q Q, Gu F, Li M, *et al.* 2012 *Chin. Phys. B 21* **8** 086101
[11] Leski A, Baraniecki R and Malachowski J 2002 *Proceedings of the* 7*th International Design Conference*, Dubrovnik
[12] Ren J L and Jiang T 2016 *Chin. Phys. B* **25** 020204
[13] Alexandrov S and Miszuris W 2016 *Acta Mechanica* **227** 813
[14] Sonato M, Piccolroaz A, Miszuris W and Mishuris G 2015 *J. Solids Struct.* 64–65 9
[15] Li Z C, Jia X P, Huang G F, Hu M H and Li Y 2013 *Chin. Phys. B* **22** 014701
[16] Liu X H, He B, Wang Z P, Tang H F, Su T and Wang Q G 2014 *Sci. Rep.* **4** 6673
[17] Yeoh O H 1993 *Rubber Chem. Technol.* **66** 754
[18] Zhang Y N 2013 *Chin. Phys. B* **22** 014214
[19] Sangpradit K, Liu H B and Dasgupta P 2011 *IEEE Transaction on Biomedical Engineering* **58** 3319
[20] Zhang H 2016 *Appl. Math. Mech. Engl. Ed.* **37** 1539
[21] Facchinetti M and Miszuris W 2016 *J. Eur. Ceram. Soc.* **36** 2295
[22] Hua D Y, Song B, Wang D F and Chen Z Y 2016 *Composite Structures* **149** 385
[23] Yang H B, Li Y, Zhao H G, Wen J H and Wen X S 2014 *Chin. Phys. B* **23** 104304
[24] Liu Q, Li S G, Wang X Y and Shi M 2016 *Chin. Phys. B* **25** 124210
[25] Sun W, Chaikof E L and Levenston M E 2008 *Journal of Biomechanical Engineering* **130** 061003
[26] Ihueze C and Mgbemena C 2014 *Journal of Scientific Research & Reports* 3 2528
[27] Yu Y Y, Li X Y, Sun B and He K P 2015 *Chin. Phys. B* **24** 068702